Composite lithium metal anode by melt infusion of lithium into a 3D conducting scaffold with lithiophilic coating

Zheng Liang[a], Dingchang Lin[a], Jie Zhao[a], Zhenda Lu[a], Yayuan Liu[a], Chong Liu[a], Yingying Lu[a], Haotian Wang[b], Kai Yan[a], Xinyong Tao[a], and Yi Cui[a,c,1]

[a]Department of Materials Science and Engineering, Stanford University, Stanford, CA 94305; [b]Applied Physics, Stanford University, Stanford, CA 94305; and [c]Stanford Institute for Materials and Energy Sciences, SLAC National Accelerator Laboratory, Menlo Park, CA 94025

Edited by Gabor A. Somorjai, University of California, Berkeley, CA, and approved January 28, 2016 (received for review September 12, 2015)

Lithium metal-based battery is considered one of the best energy storage systems due to its high theoretical capacity and lowest anode potential of all. However, dendritic growth and virtually relative infinity volume change during long-term cycling often lead to severe safety hazards and catastrophic failure. Here, a stable lithium–scaffold composite electrode is developed by lithium melt infusion into a 3D porous carbon matrix with "lithiophilic" coating. Lithium is uniformly entrapped on the matrix surface and in the 3D structure. The resulting composite electrode possesses a high conductive surface area and excellent structural stability upon galvanostatic cycling. We showed stable cycling of this composite electrode with small Li plating/stripping overpotential (<90 mV) at a high current density of 3 mA/cm^2 over 80 cycles.

Li composite | Li metal anode | melt infusion | 3D scaffold | lithiophilic

Nowadays the increasing demand for portable electronic devices as well as electric vehicles raises an urgent need for high energy density batteries. Lithium (Li) metal anode has long been regarded as the "Holy Grail" of battery technologies, due to its light weight (0.53 g/cm^3) (1), lowest anode potential (−3.04 V vs. the standard hydrogen electrode) (1), and high specific capacity (3,860 mAh/g vs. 372 mAh/g for conventional graphite anode) (1). It possesses an even higher theoretical capacity than the recently intensely researched anodes such as Ge, Sn, and Si (2–10). In addition, the demand for copper current collectors (9 g/cm^3) in conventional batteries with graphite anodes can be eliminated by employment of Li metal anodes, hence reducing the total cell weight dramatically. Therefore, Li metal could be a favorable candidate to be used in highly promising, next-generation energy storage systems such as Li–sulfur battery and Li–air battery.

The safety hazard associated with Li metal batteries, originating from the uncontrolled dendrite formation, has become a hurdle against the practical realization of Li metal-based batteries (11, 12). The sharp Li filaments can pierce through the separator with increasing cycle time, thus provoking internal short-circuiting (12). Most previous academic research to settle this bottleneck focuses on solid electrolyte interphase (SEI) stabilization/modification by introducing various additives (13–17). These electrolyte additives interact with Li quickly and create a protective layer on the Li metal surface, which helps reinforce the SEI (13–17). Furthermore, recent study in our group has also shown the employment of interconnected hollow carbon spheres (18) and hexagonal boron nitride (19) as mechanically and chemically stable artificial SEI which effectively block Li dendrite growth.

In addition to the notorious Li dendrite formation, another significant factor that contributes considerably to the battery short-circuiting is the volume change of Li metal during electrochemical cycling, which is usually overlooked (20, 21). During battery cycling, Li metal is deposited/stripped without a host material. Thus, the whole electrode suffers from a virtually infinite volume change (ratio of Li metal volume at completely charged state versus at the completely discharged state is infinite) compared with the finite volume expansion of several common anodes for lithium ion batteries such as Si (~400%) (6) and graphite (~10%) (19). As a result, the mechanical instability induced by the virtually infinite volumetric change would cause a floating electrode/separator interface as well as an internal stress fluctuation (21). However, little attention has been paid to the volume fluctuation problem of the "hostless" Li. We propose that a host scaffold to trap Li metal inside can effectively reduce the volume change of the whole electrode and therefore maintain the electrode surface.

Herein, we report a newly designed Li–scaffold composite anode and its effectiveness on addressing the safety issue of traditional hostless Li metal electrode. The preexisting scaffold serves as a rigid host with Li uniformly confined inside to accommodate the electrode-level virtually infinite volume change of Li metal during cycling. To create the composite electrode as we designed in Fig. 1*A*, we need to find a suitable porous material to host the Li metal. An ideal scaffold for Li encapsulation should have the following attributes: (*i*) mechanical and chemical stability toward electrochemical cycling; (*ii*) low gravimetric density to achieve high-energy density of the composite anode; (*iii*) good electrical and ionic conductivity to provide unblocked electron/ion pathway, enabling fast electron/ion transport; and (*iv*) relatively large surface area for Li deposition, lowering the effective electrode current density and the possibility of dendrite formation. By considering these aspects, we choose carbon-based porous materials to provide the required features. Specifically, an electrospun carbon fiber network (11) was used as an example to illustrate the capability of this composite anode to sustain the volume fluctuation and shape change during each electrochemical cycle.

How to encapsulate Li metal inside the porous carbon scaffold presents a major challenge. Compared with many of the battery electrode materials which can be fabricated via various synthetic processes, manufacturing of Li metal-based μm- and nanostructures are very difficult due to the high reactivity of Li (1, 12). Previously, studies on Li encapsulation aimed to entrap Li

Significance

This research paper presents a novel strategy for the fabrication of metal–scaffold composite materials. Particularly, molten lithium metal is infused into a surface-modified three-dimensional matrix with a "lithiophilic" coating. The resulting lithium–scaffold composite was used as battery anodes and exhibited superior performance compared with bare lithium metal anodes. Whereas the emphasis of this study is on lithium anodes, our present work opens up a direction for realization of other metal-anode–based systems. We believe the present work will contribute significantly to the energy-related field and also inspire research in other areas.

Author contributions: Z. Liang and Y.C. designed research; Z. Liang and J.Z. performed research; H.W. contributed new reagents/analytic tools; Z. Liang, D.L., J.Z., Z. Lu, Y. Liu, C.L., K.Y., X.T., and Y.C. analyzed data; and Z. Liang, Y. Liu, Y. Lu, K.Y., and Y.C. wrote the paper.

The authors declare no conflict of interest.

This article is a PNAS Direct Submission.

[1]To whom correspondence should be addressed. Email: yicui@stanford.edu.

This article contains supporting information online at www.pnas.org/lookup/suppl/doi:10.1073/pnas.1518188113/-/DCSupplemental.

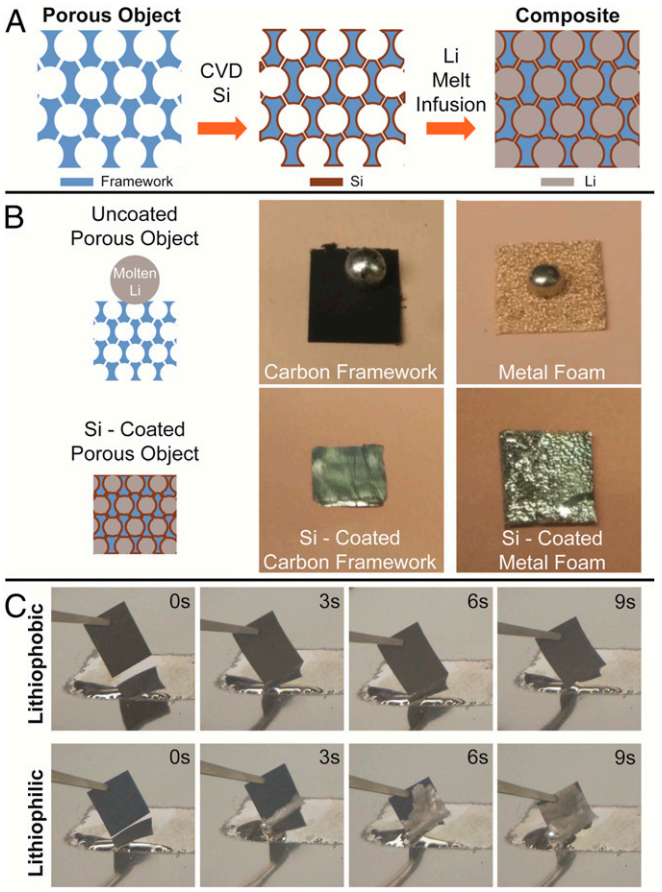

Fig. 1. Schematic and optical images of Li encapsulation by melt infusion. (*A*) Schematic illustration of the design of a Li–scaffold composite. (*B*) Li wetting property of various porous materials with and without the Si coating. (*C*) Time-lapse images of Li melt-infusion process for lithiophilic and lithiophobic materials. See the *Supporting Information* for full movies.

through electrochemical deposition. However, the lack of spatial control of the deposition and unsmooth Li surface due to dendritic Li formation impeded such progress (13, 22). Therefore, development of versatile and simple approaches for encapsulating Li inside porous carbon or other scaffold to create Li-based composite electrodes is highly desired.

Li metal possesses a low melting point of 180 °C; it would liquefy into molten Li under anaerobic atmosphere when heated to its melting point. Inspired by the fact that water could be absorbed into a hydrophilic porous structure, we develop a new strategy: melt infusion of molten Li into a "lithiophilic" matrix, which has low contact angle with liquid Li. A porous material with a thin layer of lithiophilic coating has excellent wettability with liquefied Li and thus could function as the host scaffold for Li entrapment. In this study, the aforementioned electrospun carbon fiber network modified with lithiophilic coating–silicon (Si), was used as the scaffold for Li encapsulation. Li easily and quickly flows into the fiber layer region and occupies the empty spaces between each single fiber. The resulting composite structure, denoted as Li/C, remains both mechanically and chemically stable under galvanostatic cycling; moreover, it provides a stable electrode/electrolyte interface. The effective anode current density could also be reduced due to an enlarged surface area for Li nucleation process, which in turn causes superior electrochemical performances under the same test conditions. To summarize, in contrary to the hostless Li metal, the as-proposed Li/C composite anode is able to accommodate the volume variation and therefore mitigate the potential safety hazard; moreover, the reduced current density, rooted to larger surface area, also triggers a greatly improved electrochemical performance, with stable cycling of over 2,000 mAh/g for more than 80 cycles at a high current density of 3 mA/cm^2.

Results and Discussion

Design and Fabrication of Li/C Composite Anode. Encapsulation of active materials into a conductive matrix is a well-known strategy for large-volume-change battery electrodes (10, 23–26). A design of active material–carbon framework structure has been demonstrated in a few examples, including the silicon/carbon yolk–shell structures (24), silicon/carbon pomegranate structures (10), germanium/carbon nanostructures (25), and sulfur/hollow carbon fiber hybrid structures (26). For a Li anode with virtually infinite volume change, the same design was adopted in our study. We developed an advanced Li–carbon nanofiber scaffold composite electrode which possesses a stable volume during cycling. The carbon nanofiber scaffold, with an average diameter of 196 nm (Fig. S1), was prepared by carbonization of the polyacrylonitrile (PAN) fiber (11). The schematic of this Li–carbon nanofiber scaffold design is shown in Fig. 1*A*, where the key step in the fabrication process is Li entrapment. In this design, Li was heated above its melting temperature under argon, and the resulting molten Li was absorbed into the scaffold. A thin layer of Si was coated onto the scaffold surface by chemical vapor deposition (CVD) to assist this melt-infusion process. To investigate the effectiveness of Si coating on Li wettability of a wide variety of porous materials, a molten Li droplet was placed on several different porous materials, including copper foam and carbon fiber network. As shown in Fig. 1*B*, the molten Li droplet tends to ball up and avoid contact with surfaces without any modification, suggesting an unfavorable wettability. This "lithiophobic" effect possibly originates from the lack of bonding interaction between surface (carbon or Cu) and molten Li (27, 28). For surface-modified objects, the Si coating reacts with molten Li to create a binary alloy phase–lithium silicide with some bonding interactions to pure Li (29–31). This reaction drives and guides molten Li to wet the entire surface and fill in the porous structure (28). Therefore, the Si layer functions as a lithiophilic coating promoting good wetting property of liquefied Li. Fig. 1*C* is a sequence of the time-lapse images of the Li melt-infusion process. For unmodified carbon framework, molten Li could not wet its surface. In comparison, the Si-coated carbon framework shows good wettability as molten Li quickly flows into the structure under capillary force. This process can be seen in Movies S1 and S2, which confirm, visually, the concept of "lithiophilicity" and "lithiophobicity," respectively.

Characterizations of Li/C Composite Anode. Scanning electron microscopy (SEM) and transmission electron microscopy (TEM) characterizations were performed to study the morphology of the carbon fiber as well as the spatial distribution of the Si coating. Fig. 2*A* shows the bare carbon fiber with a smooth surface, indicating the absence of coatings. The diameter of the carbon fiber is ∼200 nm (Fig. S1). In contrast, Si-coated carbon fiber displays a rough edge with Si nanoparticles homogeneously deposited on the fiber surface (Fig. 2*B*). These Si nanoparticles, with an average size of several nanometers, stack together to form a continuous, dense shell on the carbon fiber core. Fig. 2*C* is the typical TEM image of the Si layer under higher magnification. The Si shell by CVD could be observed clearly with a different contrast (lighter region) and has a thickness of ∼30 nm. The linear scan spectra again confirm the formation of a uniform Si coating on the carbon fiber surface (Fig. 2*D*). To further verify the distribution of Si inside the entire fiber layer instead of each single fiber, energy-dispersive X-ray spectroscopy (EDS) mappings of the fiber layer from the top and cross-section were performed. Fig. *F*–*J* exhibits carbon and silicon signals, revealing the presence of the Si nanoparticles throughout the whole fiber layer region. Moreover, as illustrated in Fig. 2 *F* and *I*, silicon is uniformly coated over the entire fiber layer. Therefore, this carbon fiber framework with Si homogeneously distributed could serve as an ideal matrix for Li melt infusion and ensure a conformal Li entrapment.

After Li infiltration, the resulting Li/C composite displays a smooth surface with metallic luster compared with the pristine carbon fiber network, implying Li is uniformly confined inside the

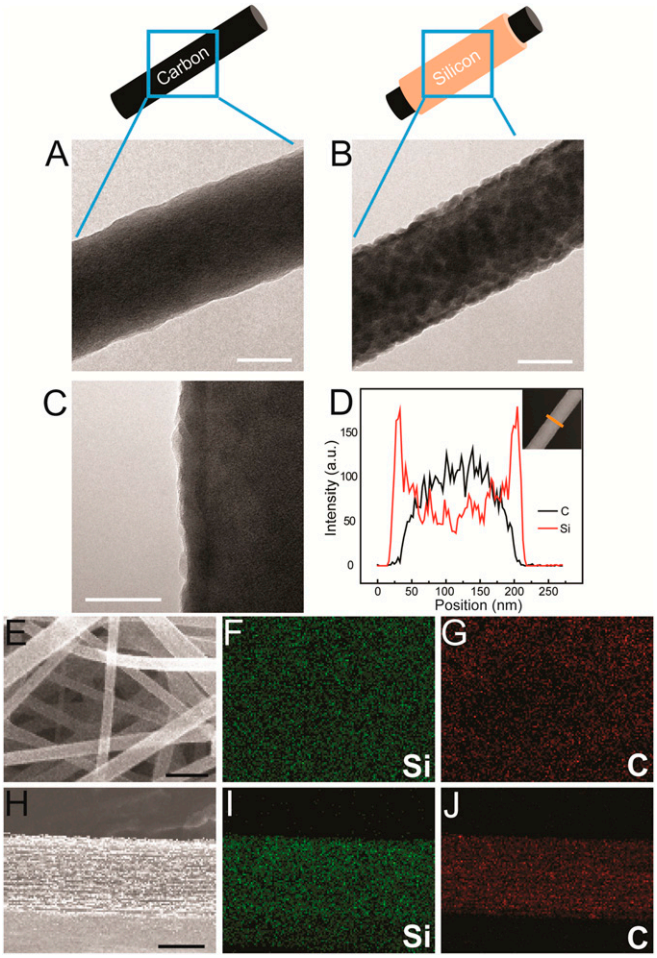

Fig. 2. Microscopic characterizations of the bare carbon fiber and Si-coated carbon fiber. (*A*) TEM image of a single uncoated carbon fiber. (*B* and *C*) TEM image (*B*) of a single Si-coated carbon fiber and its zoom-in image (*C*). (*D*, *Inset*) TEM-EDS linear scan profile obtained along the yellow line on a single fiber shown in the inset. The TEM-EDS linear scan clearly exhibits the different material compositions of inner and outer region of the fiber. (*E*–*J*) SEM-EDS characterization. Top-view SEM image (*E*) and cross-section SEM image (*H*) of the fiber layer. The corresponding elemental mapping for silicon (*F* and *I*) and carbon (*G* and *J*). (Scale bars: *A*–*C*, 100 nm; *E*, 500 nm; *H*, 50 μm.)

matrix (Fig. 3 *A* and *B*). SEM study was conducted before (Fig. 3 *C* and *D*) and after (Fig. 3 *E* and *F*) Li infusion. As illustrated in Fig. 3*C*, the carbon fiber network exhibits a three-dimensional (3D) porous structure with interconnected fibrous morphology. Furthermore, it provides a high surface area of 15.6 m^2/g (by the Brunauer–Emmett–Teller method) as well as empty inner spaces among fibers for efficient Li storage. The fiber layer has a uniform thickness of 100–120 μm (Fig. 3*D*). Fig. 3*D* (*Inset*) indicates an interconnected network which provides a continuous conductive pathway for facile ion/electron transport (8). The carbon fiber film was subjected to a simple current–voltage (*I*–*V*) measurement and the calculated through-plane resistance based on the *I*–*V* curve is ~67 Ω for a disk of 1 cm^2 and 100–120 μm thick (Fig. S2). The average sheet resistance was determined to be ~4,200 Ω/sq using a four-point meter (Fig. S3). The good electrical conductivity of this PAN-based carbon fiber network ensures a facile electron transport of the 3D backbone. Fig. 3 *E* and *F* presents the morphology of the Li/C composite material from the top and cross-section, respectively. It is clearly observed that the carbon fiber network is uniformly coated by metallic Li and the interspace pores between each single fiber were filled up with Li. The entrapped Li is restrained within the fiber layer as no Li is observed protruding beyond the fiber mat boundary. From the cross-section view, it is also concluded that the absorbed Li forms a porous structure with internal voids. The X-ray diffraction (XRD) pattern of the Li/C reveals two phases existing in the composite (Fig. 3*G*). The identified peaks are indexed as $Li_{21}Si_5$ and Li, confirming the entrapment of Li inside the scaffold. The absence of graphitic carbon signals confirms the amorphous phase of the electrospun carbon fiber. Amorphous carbon is inert to metallic lithium and provides excellent chemical/mechanical stability toward electrochemical cycling (18). Signal of lithium silicide ($Li_{21}Si_5$) is due to the reaction of Si coating with the molten Li.

Electrochemical Performances of Li/C Composite Anode. To evaluate the structural stability of the Li/C electrode during galvanostatic cycling, symmetrical coin cells (2032-type) with two identical Li/C electrodes were assembled. To standardize the test, control cells were fabricated using bare Li anode with equal thickness

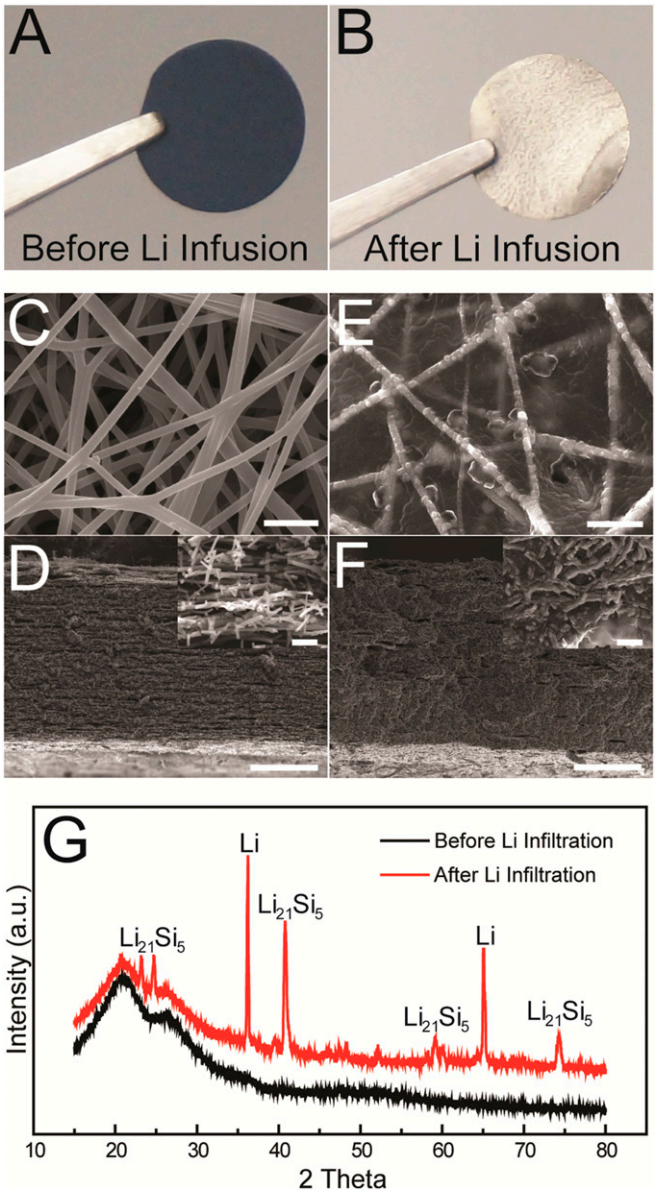

Fig. 3. SEM and XRD study of the Li/C composite material. Optical images and SEM characterizations of the modified carbon fiber network before (*A*, *C*, and *D*) and after (*B*, *E*, and *F*) Li infusion. (*Insets*) Corresponding high-magnification images. (*G*) XRD pattern collected from the modified carbon fiber before and after Li infiltration. (Scale bars: *C* and *E*, 1 μm; *D* and *F*, 50 μm; *Insets*, 2 μm.)

(~120 μm). The cells were subjected to a typical Li-stripping-plating process with current density of 1 mA/cm^2. A fixed amount of Li was stripped from the anode and then deposited back. The anode volume change could be visually pronounced by stripping a total of 10 mAh/cm^2 Li, which is equivalent to half of the anode capacity (~50% extraction). The Li/C anode shows a more stable voltage plateau compared with bare Li anodes, implying a superior interfacial stability during cycling (Fig. 4*A*) (21, 32). In addition, the Li/C anode has a much lower voltage hysteresis. The corresponding electrode thickness change during various stages of cycling is shown in Fig. 4*B*. The thickness of bare Li electrode is halved to around 60 μm after ~50% extraction of the Li, indicating a large volume change, whereas the thickness of Li/C composite remains nearly unaltered (from 116 μm to 110 μm and back to 116 μm) upon cycling, which again confirms the effectiveness of the Li/C composite anode in maintaining a virtually constant thickness. Electrode thickness was analyzed based on a summary of 15 different locations for each sample (Fig. S4).

The SEM images of electrode cross-sections during various stages of cycling are presented as Fig. 4 *C*–*H*. The shape and thickness of the control Li electrode are expected to change upon every cycle owing to the lack of a host scaffold (Fig. 4 *C*–*E*). The Li/C electrode experiences a small volume change, with an intact and stable surface (Fig. 4 *F*–*H*). Insets of Fig. 4 *G* and *H* indicate that the fibrous morphology is preserved after cycling. The carbon fiber network serves as a rigid backbone for Li to reversibly deposit into/extract from, thus ensuring an unchanged shape of the whole electrode as well as a stable interface between the electrode and electrolyte.

Morphologies of the bare Li electrode and Li/C electrode after repeated Li-plating-stripping cycles were also analyzed by SEM. Cross-sectional image of the cycled Li electrode shows an uneven surface (Fig. 4*I*), whereas the cross-section of the cycled Li/C electrode exhibits an intact electrode shape with stable interface between electrode and electrolyte (Fig. 4*J*). It should be noted that this rough surface of Li electrode after cycling originates mainly from the repeated inhomogeneous and hostless Li deposition/stripping upon cycling, inducing a noticeable mechanical pressure on the separator. Hence, the risk of battery failure is greatly enhanced. The top view of the cycled Li electrode shows Li dendrites protruding upward (Fig. S5 *A* and *B*), again confirming the overgrowth of Li filaments. For Li/C electrode, the absence of a noticeable large Li dendrite is ascribed to the effectiveness of the high-surface-area 3D matrix on reducing the actual current density (Fig. S5*C*). Therefore, the formation of dendritic Li could be suppressed to some extent. However, visible mossy Li still exists (Fig. S5*D*).

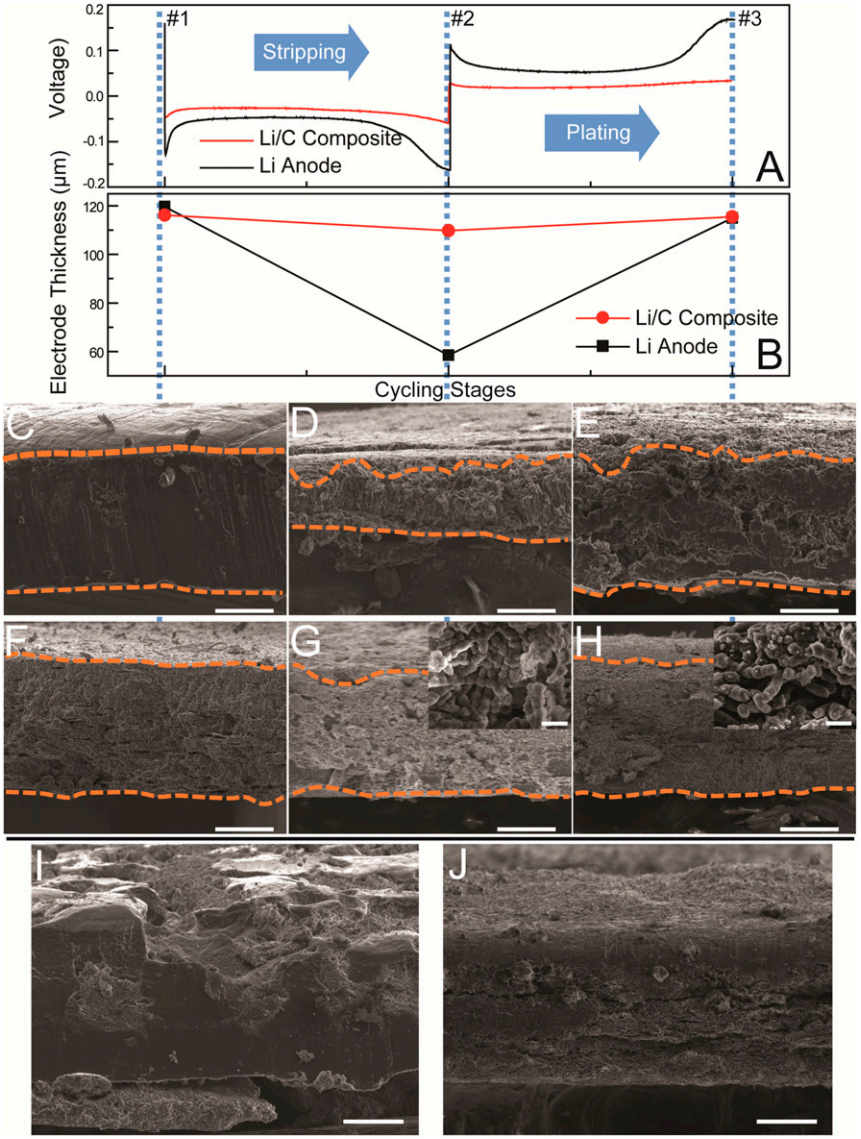

Fig. 4. Volume fluctuation of the electrode during different cycling stages. Voltage profile of a typical Li-stripping-plating process for the anode (*A*) and its corresponding thickness (*B*) at various stages of cycling. #1 corresponds to the stage before cycling; #2 corresponds to the stage after ~50% Li extraction (10 mAh/cm^2); #3 corresponds to the stage after Li plating back. (*C*–*E*) A sequence of cross-sectional SEM images showing the huge volume fluctuation and shape change of the bare Li metal anode in a typical Li-stripping-plating cycle. (*F*–*H*) A sequence of cross-sectional SEM images showing the relatively stable Li/C electrode. (*I* and *J*) Morphology study of cross-sections of bare Li electrode (*I*) and Li/C electrode (*J*) after 30 cycles at a current density of 3 mA/cm^2 for 1 mAh/cm^2. (*J*) Cross-sectional SEM image of Li/C electrode showing an unaltered shape after cycling. (Scale bars: *C*–*J*, 50 μm; *Insets*, 2 μm.)

To investigate the electrochemical performances of the advanced Li/C anode, symmetrical cells were assembled with Li/C and bare Li (control), respectively. For the electrolyte, 1 M lithium hexafluorophosphate ($LiPF_6$) in cosolvent of ethylene carbonate (EC) and diethyl carbonate (DEC) was used. Cells with bare Li electrodes and Li/C electrodes were compared in terms of plating/stripping voltage profiles (Fig. 5 *A–D*), electrochemical impedance (Fig. 5*E*), rate performance (Fig. 5*F*), and cycling behavior (Fig. 5*G*).

Fig. 5 *A–D* depicts voltage profiles of a typical Li-plating-stripping process at various test conditions (0.5 mA/cm^2 and 3 mA/cm^2 for 0.5 mAh/cm^2 and 1 mAh/cm^2, respectively). These voltages curves for bare Li electrode consistently show significant dips and bumps whereas those for Li/C electrode exhibit a flat and stable plateau. It is thus concluded that Li incorporation/extraction for Li/C is more easily initiated and maintained compared with a bare Li electrode (21). Because Li is plated/stripped on/from Li itself, the nucleation barrier originating from lattice mismatch is minimized (33). Therefore, the unstable voltage curves for bare Li anodes can be ascribed to the variation of electrode surface and shape over time (32). An ac impedance test was performed to examine the interfacial resistance in a symmetrical cell configuration. The measurement was conducted on both pristine electrodes and those after the first cycle of Li plating/stripping to eliminate the influence of surface impurities (32). The interfacial impedance for pristine Li and Li/C, as indicated by the semicircle at high frequency, stays at ∼450 Ω and ∼60 Ω, respectively (Fig. 5*E*). For Li and Li/C electrode after the first cycle, the interfacial impedance reaches ∼90 Ω and ∼40 Ω, respectively (Fig. 5*E*). The larger impedance for the control Li suggests that the nonuniform and hostless Li plating/stripping has resulted in poor Li ion transport. The reduced Li ion transport resistance for Li/C electrode is in accordance with the smaller cycling overpotential and more stable voltage curve in Fig. 5 *A–D*.

Fig. 5*F* presents the rate behavior of the Li/C composite. Voltage hysteresis is plotted versus cycle numbers under various current densities ranging from 0.5 to 10 C. Voltage hysteresis is defined as the sum of overpotential for Li deposition and Li dissolution. As illustrated in Fig. 5*F*, Li/C electrode delivers a steadily increasing voltage hysteresis of 40, 70, 190, 300, and 380 mV at 0.5, 1, 3, 5, and 10 C, respectively. Meanwhile, the bare Li electrode delivers a much larger voltage polarization of 150, 180, 330, 550, and 870 mV under the same test conditions. This good rate capability of Li/C reveals facile ion/electron transport, owing to the existence of an unblocked ion/electron conductive pathway inside the Li/C composite (21, 32). Fig. 5*G* shows the long-term cycling profile of the symmetrical coin cells. For the Li/C electrode, it can cycle stably for more than 80 cycles under a high current rate of 3 mA/cm^2. The voltage plateau is stable at each charge–discharge process. Even after 80 cycles, the cell shows no evidence of dendrite-induced failure, whereas for the bare Li electrode, the voltage hysteresis gradually increases with increasing cycle time until an abrupt drop (Fig. 5*G*). This sudden voltage change could be caused by excessive formation and continuous building up of SEI, followed by the breaking down of separator (33–35). It is evident that cells with a hostless bare Li electrode exhibit a predominantly and irregularly fluctuating voltage profile which is consistent with the cell failure by a dendrite-induced short-circuit. Moreover, despite the fact that introducing a matrix could reduce the overall capacity of the entire composite anode to some extent, our proposed Li/C composite electrode is still able to

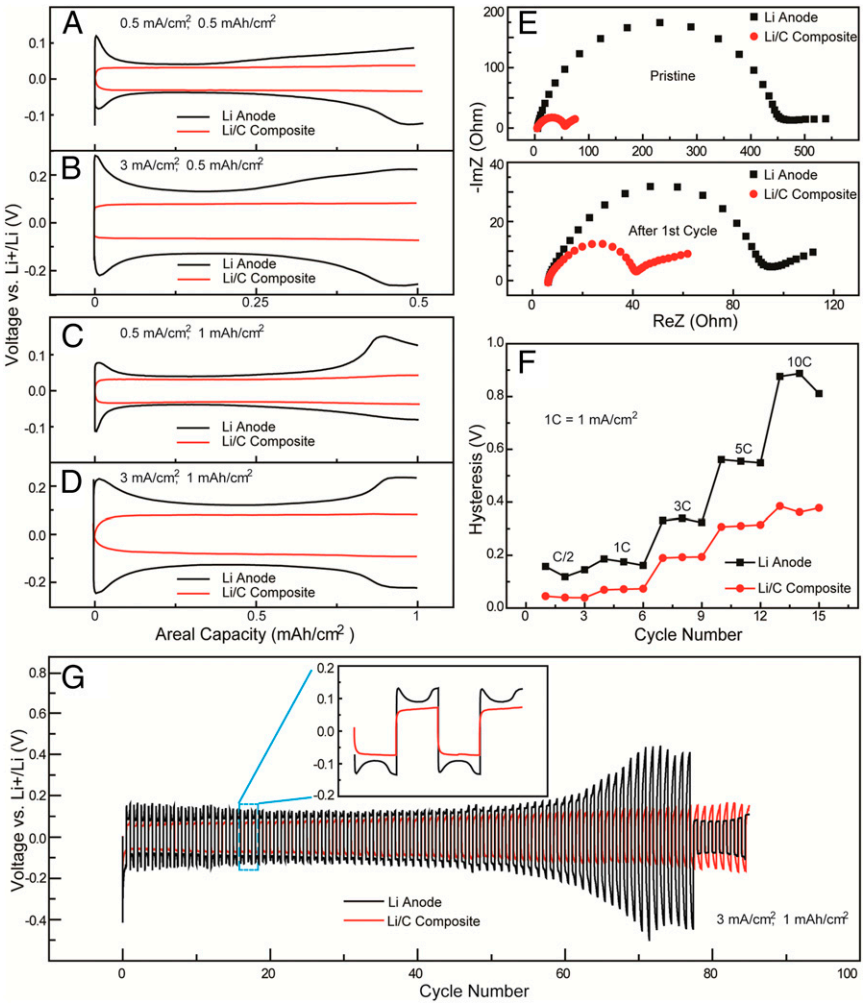

Fig. 5. Electrochemical performances of Li symmetrical cells and Li/C symmetrical cells. (*A–D*) Typical voltage profiles of Li-plating-stripping process with current density of 0.5 mA/cm^2 for 0.5 mAh/cm^2 (*A*), 3 mA/cm^2 for 0.5 mAh/cm^2 (*B*), 0.5 mA/cm^2 for 1 mAh/cm^2 (*C*), and 3 mA/cm^2 for 1 mAh/cm^2 (*D*). (*E*) Impedance spectroscopy of Li/C and bare Li electrode. (*F*) Comparison of voltage hysteresis of the Li-plating-stripping process for Li/C and Li electrode under various current rates. (*G*) Long-term cycling performance of Li/C and bare Li symmetrical cells with current density of 3 mA/cm^2 for a total of 1 mAh/cm^2.

deliver a competitive specific capacity of over 2,000 mAh/g (Fig. S6), which is more than half of the theoretical capacity for lithium metal and significantly higher than carbonaceous anodes. The measured volumetric capacity is around 1,900 mAh/cm^3 (Fig. S6), which indicates a high porosity of the carbon fiber matrix (~90%).

Conclusion

We have introduced a facile melt-infusion approach to effectively encapsulate Li inside a porous host scaffold. The infiltrated Li uniformly confined within the matrix creates a Li composite material. It can deliver a high capacity of around 2,000 mAh/g (gravimetric) or 1,900 mAh/cm^3 (volumetric) as stable anodes for Li metal batteries. This novel design affords remarkable battery performance with a low interfacial impedance, stable voltage profile and long cycle life, due to its high conductive surface area, stable electrolyte/electrode interface, and negligible volume fluctuation. Compared with a hostless Li metal electrode, this Li/C composite electrode has multiple advantages and therefore can open a new avenue for solving the intrinsic problems of Li metal-based batteries.

Methods

Si-Coated Carbon Nanofiber Fabrication. PAN, polyvinylpyrrolidone (PVP), and dimethylformamide (DMF), are all commercially available from Sigma-Aldrich. A total of 0.5 g PAN (M_w = 150,000) and 0.5 g PVP (M_w = 1,300,000) were added into 10 mL DMF. The as-prepared solution was stirred vigorously at 80 °C for 6 h. The solution was electrospun into nanofiber with the following parameters: 18-cm nozzle-to-collector distance, 15-kV voltage, 0.3-mL/h pump rate, 9 cm × 9-cm graphite paper collector size. After 40 h of electrospinning, the as-prepared fiber mat was stabilized in air at 300 °C for 2 h in a box furnace (Thermo Electron Corporation). The oxidized fiber was then transferred to a tube furnace (Thermo Electron Corporation) to be carbonized at 700 °C under argon atmosphere for 3 h with a heating rate of 5 °C/min. Si was coated onto the carbon fiber network via CVD with the following parameters: 100-sccm silane flow rate, 30-torr pressure, 490 °C for 30 min.

Li Infiltration. The surface of the Li metal foil was polished to remove the impurities. For the Li melt-infusion process, Li was heated over 300 °C on a nickel sheet under argon atmosphere. The oxygen level should be kept below 0.1 ppm to ensure little oxide on the molten Li surface. Different porous materials were dipped into the molten Li and held until Li flowed into the structure completely.

Characterization. SEM study and elemental mapping were conducted using an FEI XL30 Sirion SEM. TEM characterization and linear scan were performed with an FEI Tecnai G2 F20 X-TWIN transmission electron microscope. XRD was carried out using an X-ray diffractometer (X'Pert Pro, PANalytical) with Cu Kα radiation. Specific surface area of the carbon nanofiber was determined by the Brunauer–Emmett–Teller method based on nitrogen gas adsorption, using a Micromeritics ASAP 2020 analyzer. The samples (~100 mg in total) were degassed at 150 °C for 24 h before analysis.

Electrochemical Measurements. Li metal and Li/C composite were cut into 1-cm^2 disks by a punch machine (MTI). Symmetrical MTI type-2032 coin cells were assembled with two identical electrodes inside an argon-filled glove box (MB-200B, Mbraun); 1 M $LiPF_6$ in EC/DEC (1:1 vol %) was used as electrolyte. Battery testing was carried out with a 96-channel battery tester (Arbin Instruments). Electrochemical impedance was probed at room temperature over the frequency from 0.1 Hz to 200 kHz on an electrochemical workstation (BioLogic Science Instruments, VMP3). To perform the *I–V* measurement, carbon fiber film (1 cm^2, 100–120 μm thick) was sandwiched between two copper foils connecting to the electrochemical station (BioLogic Science Instruments, VMP3). Scan rate was 50 mV/s, within the range of –2–2 V. Sheet resistance of the carbon fiber film was measured by the four-point probe technique, using a four-point meter (Rchek, model RC2175). The samples were cut into proper size (rectangle, 1 cm × 3 cm, thickness of ~100–120 μm) and the average sheet resistance is based on 20 samples.

Calculation of Gravimetric Specific Capacity of the Li/C Electrode. The gravimetric specific capacity of the Li metal anode is 3,860 mAh/g. The weight percentage of Li in the composite is ~60% (Table S1), and the corresponding gravimetric specific capacity is 3,860 mAh/g × 60% = 2,316 mAh/g. The calculated specific capacity (2,316 mAh/g) is close to the measured specific capacity (2,061 mAh/cm^3) obtained through a simple electrochemical stripping (Fig. S6).

ACKNOWLEDGMENTS. Y.C. acknowledges the support from the Assistant Secretary for Energy Efficiency and Renewable Energy, Office of Vehicle Technologies of the US Department of Energy under the Battery Materials Research (BMR) program.

1. Xu W, et al. (2014) Lithium metal anodes for rechargeable batteries. *Energy Environ Sci* 7(2):513–537.
2. Chan CK, Zhang XF, Cui Y (2008) High capacity Li ion battery anodes using Ge nanowires. *Nano Lett* 8(1):307–309.
3. Lee KT, Jung YS, Oh SM (2003) Synthesis of tin-encapsulated spherical hollow carbon for anode material in lithium secondary batteries. *J Am Chem Soc* 125(19):5652–5653.
4. Chan CK, et al. (2008) High-performance lithium battery anodes using silicon nanowires. *Nat Nanotechnol* 3(1):31–35.
5. Wang C, et al. (2013) Self-healing chemistry enables the stable operation of silicon microparticle anodes for high-energy lithium-ion batteries. *Nat Chem* 5(12):1042–1048.
6. Wu H, Cui Y (2012) Designing nanostructured Si anodes for high energy lithium ion batteries. *Nano Today* 7(5):414–429.
7. Yao Y, Liu N, McDowell MT, Pasta M, Cui Y (2012) Improving the cycling stability of silicon nanowire anodes with conducting polymer coatings. *Energy Environ Sci* 5(7):7927–7930.
8. Wu H, et al. (2012) Stable cycling of double-walled silicon nanotube battery anodes through solid-electrolyte interphase control. *Nat Nanotechnol* 7(5):310–315.
9. Yao Y, et al. (2011) Interconnected silicon hollow nanospheres for lithium-ion battery anodes with long cycle life. *Nano Lett* 11(7):2949–2954.
10. Liu N, et al. (2014) A pomegranate-inspired nanoscale design for large-volume-change lithium battery anodes. *Nat Nanotechnol* 9(3):187–192.
11. Liang Z, et al. (2015) Polymer nanofiber-guided uniform lithium deposition for battery electrodes. *Nano Lett* 15(5):2910–2916.
12. Kim H, et al. (2013) Metallic anodes for next generation secondary batteries. *Chem Soc Rev* 42(23):9011–9034.
13. Takehara Z (1997) Future prospects of the lithium metal anode. *J Power Sources* 68(1):82–86.
14. Stark JK, Ding Y, Kohl PA (2011) Dendrite-free electrodeposition and reoxidation of lithium-sodium alloy for metal-anode battery. *J Electrochem Soc* 158(10):A1100–A1105.
15. Mogi R, et al. (2002) Effects of some organic additives on lithium deposition in propylene carbonate. *J Electrochem Soc* 149(12):A1578–A1583.
16. Abraham KM, Foos JS, Goldman JL (1984) Long cycle-life secondary lithium cells utilizing tetrahydrofuran. *J Electrochem Soc* 131(9):2197–2199.
17. Ishikawa M, Yoshitake S, Morita M, Matsuda Y (1994) In situ scanning vibrating electrode technique for the characterization of interface between lithium electrode and electrolytes containing additives. *J Electrochem Soc* 141(12):L159–L161.
18. Zheng G, et al. (2014) Interconnected hollow carbon nanospheres for stable lithium metal anodes. *Nat Nanotechnol* 9(8):618–623.
19. Yan K, et al. (2014) Ultrathin two-dimensional atomic crystals as stable interfacial layer for improvement of lithium metal anode. *Nano Lett* 14(10):6016–6022.
20. Cheng XB, Peng HJ, Huang JQ, Wei F, Zhang Q (2014) Dendrite-free nanostructured anode: Entrapment of lithium in a 3D fibrous matrix for ultra-stable lithium-sulfur batteries. *Small* 10(21):4257–4263.
21. Kang HK, Woo SG, Kim JH, Lee SR, Kim YJ (2015) Conductive porous carbon film as a lithium metal storage medium. *Electrochim Acta* 176(10):172–178.
22. Aurbach D, Zinigrad E, Cohen Y, Teller H (2002) A short review of failure mechanisms of lithium metal and lithiated graphite anodes in liquid electrolyte solutions. *Solid State Ion* 148(3):405–416.
23. Liang Z, et al. (2014) Sulfur cathodes with hydrogen reduced titanium dioxide inverse opal structure. *ACS Nano* 8(5):5249–5256.
24. Liu N, et al. (2012) A yolk-shell design for stabilized and scalable Li-ion battery alloy anodes. *Nano Lett* 12(6):3315–3321.
25. Seng KH, Park MH, Guo ZP, Liu HK, Cho J (2012) Self-assembled germanium/carbon nanostructures as high-power anode material for the lithium-ion battery. *Angew Chem Int Ed Engl* 51(23):5657–5661.
26. Zheng G, Yang Y, Cha JJ, Hong SS, Cui Y (2011) Hollow carbon nanofiber-encapsulated sulfur cathodes for high specific capacity rechargeable lithium batteries. *Nano Lett* 11(10):4462–4467.
27. Schofield SR, et al. (2013) Quantum engineering at the silicon surface using dangling bonds. *Nat Commun* 4:1649.
28. Fiflis P, et al. (2014) Wetting properties of liquid lithium on select fusion relevant surfaces. *Fusion Eng Des* 89(12):2827–2832.
29. Cloud JE, et al. (2014) Lithium silicide nanocrystals: Synthesis, chemical stability, thermal stability, and carbon encapsulation. *Inorg Chem* 53(20):11289–11297.
30. Kim H, Chou CY, Ekerdt JG, Hwang GS (2011) Structure and properties of Li-Si alloys: A first-principles study. *J Phys Chem B* 115(5):2514–2521.
31. Radin MD, Rodriguez JF, Tian F, Siegel DJ (2012) Lithium peroxide surfaces are metallic, while lithium oxide surfaces are not. *J Am Chem Soc* 134(2):1093–1103.
32. Duan B, et al. (2013) Li-B alloy as anode material for lithium/sulfur battery. *ECS Electrochem Lett* 2(6):A47–A51.
33. Bieker G, Winter M, Bieker P (2015) Electrochemical in situ investigations of SEI and dendrite formation on the lithium metal anode. *Phys Chem Chem Phys* 17(14):8670–8679.
34. Lu Y, Tu Z, Archer LA (2014) Stable lithium electrodeposition in liquid and nanoporous solid electrolytes. *Nat Mater* 13(10):961–969.
35. Lu Y, Korf K, Kambe Y, Tu Z, Archer LA (2014) Ionic-liquid-nanoparticle hybrid electrolytes: Applications in lithium metal batteries. *Angew Chem Int Ed Engl* 53(2):488–492.